

# Seismic Sensor Misorientation Measurement Using P-Wave Particle Motion: An Application to the NECsaids Array

by Xin Wang, Qi-Fu Chen, Juan Li, and Shengji Wei

## ABSTRACT

Seismic sensor orientation is one of the most critical parameters for modern three-component seismological observation. However, this parameter is easily subject to error imposed by strong magnetic anomalies near the station or by human error in declination calibration. It is therefore very important to inspect and correct for sensor misorientation before utilizing three-component waveform data. In this study, we measured the epoch-dependent sensor misorientation for our temporary seismic array (NorthEast China Seismic Array to Investigate Deep Subduction, or NECsaids) by analyzing *P*-wave particle motions. We applied principal component analysis and the minimizing transverse energy method to study earthquakes with epicentral distance between 5° and 90° to estimate the sensor misorientation. Our results show high consistency with the direct gyrocompass measurements, with a correlation coefficient of 0.95. Our statistical analysis suggests that we can estimate robust sensor misorientation utilizing 10 earthquakes with high signal-to-noise ratio records and highly linear *P*-wave polarizations. We also find that the influence of anisotropy or a dipping interface produces a periodical pattern with back azimuth and is relatively small for our misorientation estimation. By analyzing the amplitude change of synthetic seismograms due to misorientation and taking into account the influence of anisotropy and dipping interfaces, as well as the measurement errors, we expect engineers to be able to orient seismic sensors with error smaller than 3°.

*Online Material:* Table of the NECsaids Array sensor misorientation estimation.

## INTRODUCTION

Many modern seismological studies rely on precise three-component waveform observations, such as focal-mechanism inversions, shear-wave splitting, receiver function, normal mode and surface-wave analysis. The recorded horizontal com-

ponents are often rotated to a radial–transverse (R–T) coordinate to isolate the *P*–*SV* and *SH* energy. However, the back azimuth, which is required for R–T rotation, is easily subject to misalignment between the station sensor’s north component (such as BHN) and the true north direction (Fig. 1). If there is a sensor misorientation, the resulting R–T rotation will deviate from the proper rotated system, which will affect the accuracy and reliability of the following seismological studies.

Typically, a field engineer determines the sensor orientation during installation by finding true north, transferring a reference line, and measuring the orientation of the sensor relative to the reference line (Ringler *et al.*, 2013). Using a fiber-optic gyrocompass to find true north and a sunshot (such as theodolite or Global Positioning System) to transfer the reference line is one of the most accurate methods to assess the sensor orientation. Unfortunately, the cost and weight of such equipment restricts their availability for many temporary seismic experiments. The most economic and common way to determine north is to use a magnetic compass with a site-specific declination correction and then align the instrument to north using an orientation rod or a ruler. However, this method has potentially large errors due to the influence of magnetic material near the station (e.g., ore deposit, steel, or the sensor itself) or an incorrect declination. Significant errors may also occur when transferring the north line to the instrument with an orientation rod or ruler, particularly for the number of turns required to transfer north from the surface to the sensor location. In addition, the sensors are often reoriented during maintenance visits, reinstallation, or seismometer replacements, which could reintroduce misorientation. Considerable error may be introduced in the particular case in which no physical marks are present near the sensor that may be used as a reference during reinstallation.

The inspection and correction of sensor misorientation has been a basic and fundamental project for seismologists, making use of methods such as the analysis of the polarizations of long-period Rayleigh waves (Laske, 1995; Zha *et al.*, 2013; Rueda and Mezcuca, 2015) and *P* waves (Schulte-Pelkum *et al.*, 2001; Niu and Li, 2011), as well as calculating the correlation

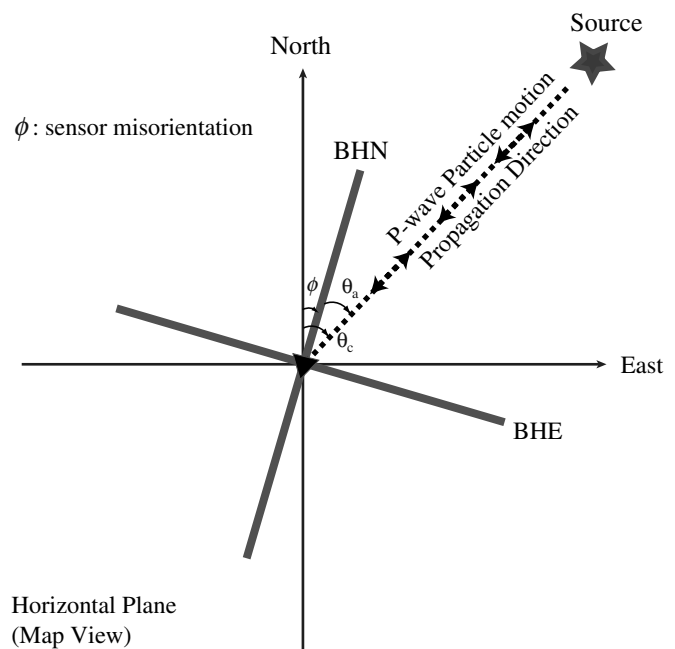
between data and synthetic seismograms (Ekström and Busby, 2008). For example, by studying the polarization of intermediate-period surface waves, Laske (1995) reported 10 of the Global Seismographic Network stations had 10° or more misorientation. By analyzing the time-dependent misorientation, Rueda and Mezcuca (2015) found that 32% of the Spanish Broadband National Network stations had larger than 15° misorientation during operation. Niu and Li (2011) investigated the direct *P*-wave particle motion and found that 270 stations of the ~800 stations in China Digital Seismic Network had misorientations larger than 8°. For the USArray Transportable Array and Backbone stations (473 stations by December 2007), 10.3% of the stations deviated 7° or more from their reported orientation (Ekström and Busby, 2008).

These studies suggest that even for national and global seismic networks operated by experienced field engineers, sensor misorientation is a universal issue. Therefore, greater attention is necessary when establishing sensor orientation, particularly for temporary seismic experiments. In this study, we calculated the misorientation of our temporary seismic array (NorthEast China Seismic Array to Investigate Deep Subduction, or NECsads) by analyzing *P*-wave particle motion; we then compared our results with gyrocompass measurements. We discussed various parameters that could improve the accuracy of the fast-automatic process. Finally, we used synthetic seismograms to investigate the effect of misorientation in distorting waveforms and consider additional factors (seismic anisotropy and dipping interfaces) that may influence the measurement of misorientation. This study will help to standardize operation in installing permanent or temporary stations, as well as provide a well-documented epoch-dependent analysis of the misorientation of existing databases.

## METHOD

The polarization of the *P* wave, when propagating in a homogeneous and isotropic layered medium, is linear (Lay and Wallace, 1995). The particle motion of the *P* wave is along the direction of ray path. The surface projection of a seismic ray, which connects the source and the receiver along the great circle path, defines the back azimuth ( $\theta_c$ ) at the station (Fig. 1). Accordingly, *P*-wave energy is then distributed between the vertical and radial components (*P*-*SV* system) and is absent in the transverse component (*SH* system). Our misorientation analysis is based on these basic features, which have been well confirmed by analysis of long-period seismic records (Bormann, 2012). As shown in Figure 1, the sensor misorientation  $\phi$  is defined as the clockwise angle between the geographic true north direction and the sensor's north component.

For a single seismic trace, the polarization of *P* waves can be found by calculating the eigenvalues and eigenvectors for the covariance matrix over a time window spanning the first few seconds following the direct *P* arrival (Jurkevics, 1988; Rost and Thomas, 2002; Fontaine *et al.*, 2009). The back azimuth and the incident angle of the *P* wave are related to the eigenvector with the largest eigenvalue. If we assume that the three



▲ **Figure 1.** The coordinate systems and wave-propagation direction (particle-motion direction or polarization) from source to station in an ideal Earth. The clockwise deviation angle between geographic north (north) and sensor orientation (BHN) is defined as the misorientation ( $\phi$ ).  $\theta_c$  is the back azimuth, calculated from source–station geometry, and  $\theta_a$  is the back azimuth measured from *P*-wave particle motion (modified from Niu and Li, 2011).

components are mutually orthogonal (true orthogonality is guaranteed by design for most modern broadband seismometers), the back azimuth can be estimated simply by solving the eigenproblem for the two horizontal components (Niu and Li, 2011). The covariance matrix **C** for the two horizontal components with a time window ( $t_1, t_2$ ) around the direct *P* wave can be written as

$$\mathbf{C} = \begin{pmatrix} c_{NN} & c_{NE} \\ c_{NE} & c_{EE} \end{pmatrix}, \quad c_{ij} = \int_{t_1}^{t_2} u_i(t)u_j(t)dt \quad i, j = N, E \quad (1)$$

in which  $u(t)$  is the horizontal component from the seismic data. The back azimuth can be found by solving the eigenproblem of  $|\mathbf{C} - \lambda\mathbf{I}| = 0$ , with  $\mathbf{I}$  being the  $2 \times 2$  identity matrix,  $\lambda$  the eigenvalues, and  $\mathbf{V}$  the corresponding eigenvectors. The eigenvalues can be written as

$$\lambda = \frac{1}{2}[c_{NN} + c_{EE} \pm \sqrt{(c_{NN} - c_{EE})^2 + 4c_{NE}^2}]. \quad (2)$$

In the absence of noise, the covariance matrix **C** will only have one nonzero eigenvalue, and the *P*-wave particle motion will be linear. In the presence of noise, **C** has two nonzero eigenvalues such that the ratio of the two defines the linearity

of the particle motion and is also an index for the noise level (Niu and Li, 2011). The back azimuth is related to the eigenvector with the largest eigenvalue,

$$\theta_a = \cot^{-1} \frac{c_{EE} - c_{NN} + \sqrt{(c_{NN} - c_{EE})^2 + 4c_{NE}^2}}{2c_{NE}}. \quad (3)$$

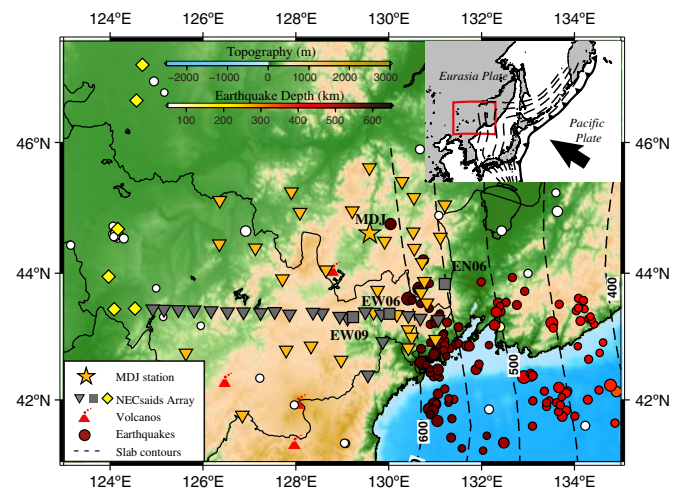
This method for determining the back azimuth is called principal component analysis (PCA), which is widely used in single-station *P*-wave earthquake early warning (Lockman and Allen, 2005; Noda *et al.*, 2012). We use this simple method for waveform quality control and as a primary estimation. For a series of earthquakes recorded by one station, we define the average value  $\varphi_{\text{PCA}}$  as the misorientation measurement from the PCA method.

As mentioned above, the direct *P*-wave energy recorded on the transverse component should be close to zero for an ideal Earth. Therefore, we can also estimate the angle by rotating the northeast coordinate system to the R-T coordinate under the guiding principle that the best angle will minimize the *P*-wave energy on the transverse component. Here, we use the signal-to-noise ratio (SNR)-weighted-multievent method (Niu and Li, 2011) to grid-search the best  $\varphi$  to minimize the energy in the transverse component from a suite of events recorded at one station. We choose events with magnitude larger than 5.5 and epicentral distance range of  $5^\circ$ – $90^\circ$ . We define the value  $\varphi_{\text{min T}}$  as the misorientation measurement from the minimizing transverse energy method, which has been proven to be effective in obtaining robust estimation of sensor orientation (Niu *et al.*, 2007; Niu and Li, 2011).

## APPLICATION TO THE NECSAIDS ARRAY

Over the period 2011–2015, we installed around 60 temporary broadband seismic stations (NECSAIDS array) in northeast China (Fig. 2), though not all stations were functioning concurrently. The NECSAIDS array was set up to study the details of the upper-mantle structure beneath northeast China to better understand the geometry and deep subduction process of the Pacific slab. These stations were emplaced with two nearly orthogonal profiles (north–south line and east–west line; stations are correspondingly named NS or EW), with average station spacing of about 15–30 km, and with other sporadic stations around these profiles (named as EN stations). All seismometers are either STS-2/2.5 or Trillium T40/T120.

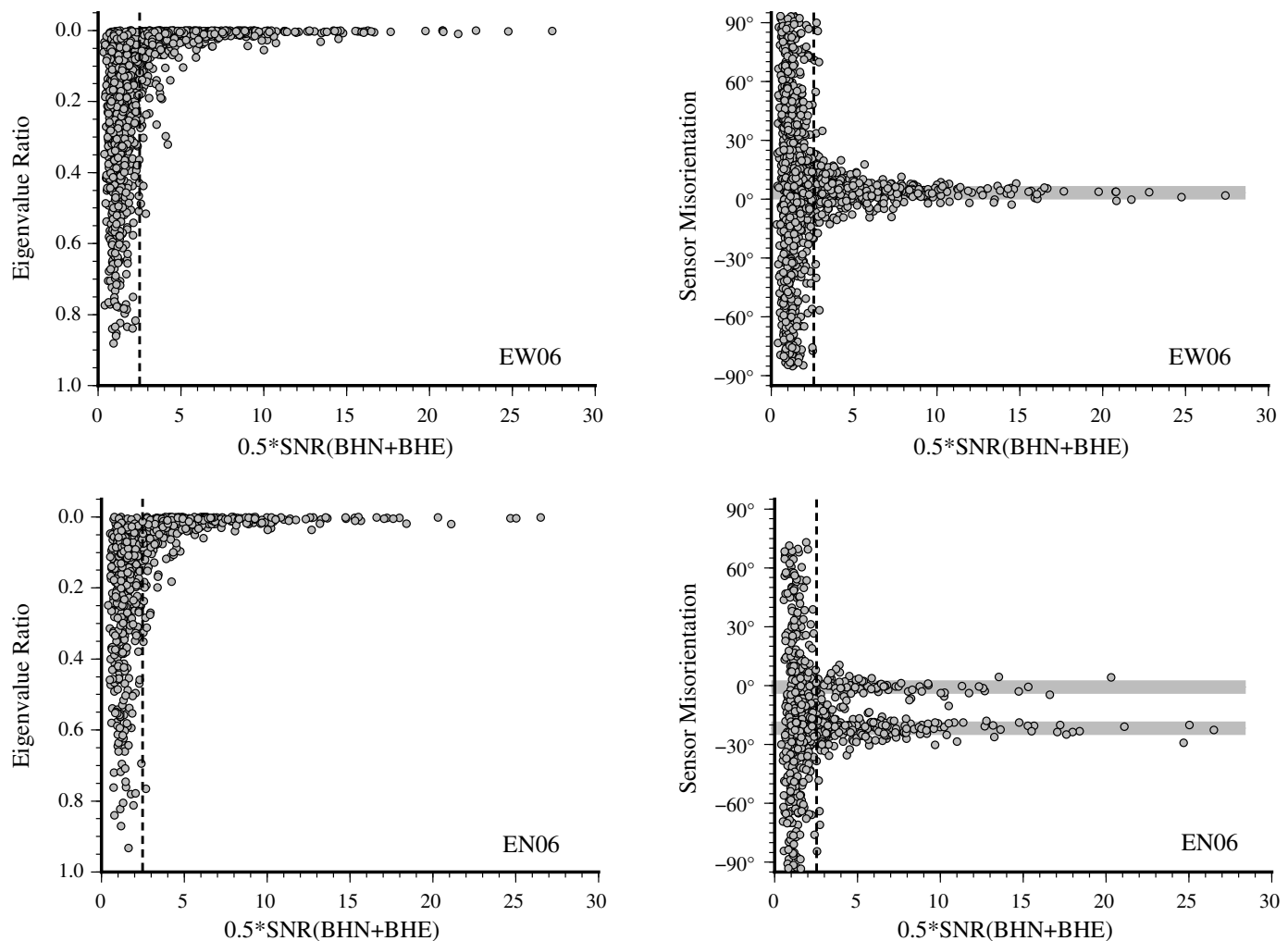
During the initial installation, the sensor orientations were determined by magnetic compass with a site-specific declination correction. As mentioned above, this method for finding true north could potentially have large errors due to the influence of magnetic material near the stations or an incorrect declination (Ringer *et al.*, 2013). During the period of observation, we inspected and serviced seismic stations about every four months, including changing the recording medium, getting metadata, and conducting necessary instrument maintenance. Sometimes we need to reinstall or replace seismometers, which can potentially change the orientations. To search for pos-



▲ **Figure 2.** The NECSAIDS temporary seismic stations (triangles and squares). The circles represent the earthquakes that occurred in this region from the International Seismological Centre catalog (see Data and Resources) from 13 April 1960 to 6 January 2016, colored by their depths. We analyzed the possible sensor misorientation of all these stations using the *P*-wave particle motion method. Among them, the station sensor misorientations verified by fiber-optic gyrocompass on May 2015 are shown as gray triangles and squares. The diamonds represent stations installed in August 2014 or May 2015. The color version of this figure is available only in the electronic edition.

sible misorientations in the NECSAIDS Array, we applied the two methods described above to analyze the epoch-dependent (each maintenance begins a new station epoch) misorientations at each station. The process for obtaining the sensor misorientation consists of three major steps: (1) data preparation and preprocessing, (2) data quality control, and (3) measuring the epoch-dependent sensor misorientation.

The first stage consists of preparing and preprocessing the waveform data. We selected earthquakes with magnitude larger than 5.5 and epicentral distance range of  $5^\circ$ – $90^\circ$ . We select such a broad range of epicentral distances for several reasons. First, we can check our results for internal consistency with regard to distance. We find that the results from regional earthquakes are not biased with respect to those from the teleseismic distance, which indicates that *P*-wave triplication has less effect on our measurements. Second, at these distances, the effects of epicentral mislocation can be ignored. For events with epicentral distance less than  $5^\circ$ , the horizontal location uncertainty in the U.S. Geological Survey (USGS) catalog may influence the estimation of back azimuth, which later affects the measurement of the misorientation (e.g., with 20 km mislocation, the maximum difference between the calculated back azimuth and the true back azimuth is around  $2^\circ$  for an epicentral distance of  $5^\circ$  but decreases to  $0.3^\circ$  for epicentral distance of  $60^\circ$ ). Third, being able to use events occurring at epicentral distances ranging from  $5^\circ$  to  $90^\circ$  notably increases azimuthal coverage of incoming rays. This helps us to rule out the influence of seismic anisotropy and dipping interfaces (see Discussion). Finally, our



▲ **Figure 3.** Single-earthquake principal component analysis (PCA): eigenvalue ratio and single-earthquake misorientation estimation as a function of average signal-to-noise ratio (SNR) for EW06 and EN06 stations. The dashed line indicates  $0.5 \times \text{SNR}_{(\text{BHN}+\text{BHE})} = 2.5$ . The eigenvalue ratio is defined as the ratio between minimum and maximum eigenvalue. With an automatic waveform quality control using SNR and eigenvalue ratio, the remaining single-earthquake measurements have much smaller scatter. The gray lines on the right figures highlight the dominant estimations.

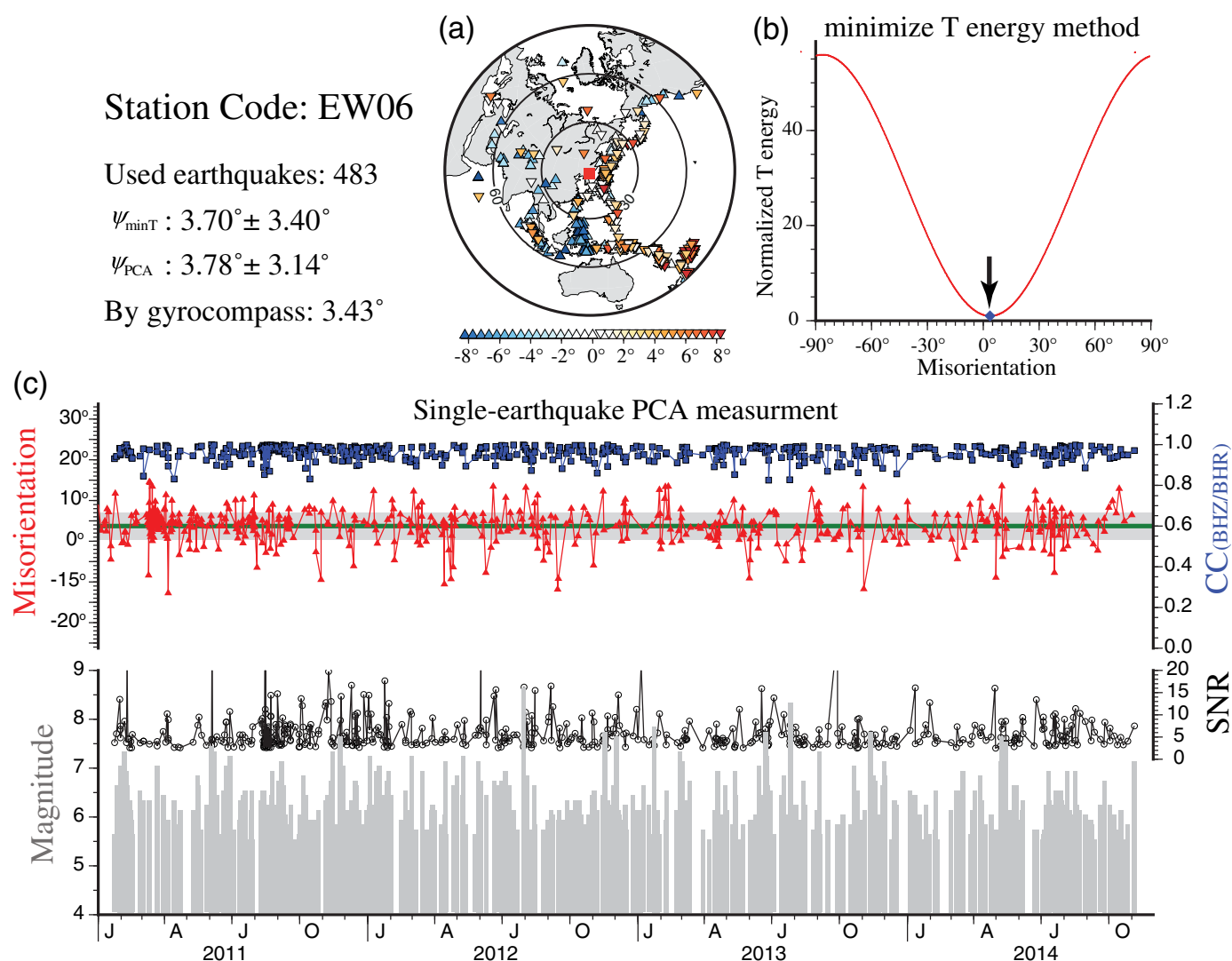
distance ranges cover the ranges of both [Niu and Li \(2011\)](#) and [Fontaine \*et al.\*, \(2009\)](#), which are based on epicentral distances from 30° to 90° and from 10° to 70°, respectively. Next, we removed the instrumental responses, converted the data to ground velocity, and applied a zero-phase band-pass filter of 5–50 s to the horizontal components. We then calculated the theoretical direct *P*-wave travel times based on the 1D IASP91 model ([Kennett and Engdahl, 1991](#)) and windowed the waveforms between –10 s and 10 s relative to each predicted arrival.

The second stage of data processing is data quality control. Careful data quality control procedures are necessary to filter out low-quality waveforms to ensure an accurate estimate of misorientation. The selection is based on single-earthquake waveform SNR and PCA analysis. We calculated the SNR of each waveform and only selected those that had  $0.5 \times \text{SNR}_{(\text{BHN}+\text{BHE})} \geq 2.5$  for later analysis. We also calculated the ratio of the eigenvalues for each event and removed those with ratio  $\lambda_{\min}/\lambda_{\max} > 0.2$ .

The remaining waveforms have highly linearized *P*-wave polarization. After the automatic quality control, the remaining measurements show a much smaller scatter for an individual station (Fig. 3). Notice that there are two dominant single-earthquake PCA estimations in EN06 station (Fig. 3), which suggests the sensor orientation changed during the observation period. The automatic data quality control will enhance the accuracy of fast-automatic analysis.

The third phase of processing is to estimate the average misorientation using the PCA method ( $\varphi_{\text{PCA}}$ ) and the minimizing transverse energy method ( $\varphi_{\min T}$ ). An example is shown in Figure 4c, in which triangles represent the single-earthquake PCA measurement sorted by date and with earthquake magnitude (gray bars) and SNR (black open circles) shown in the lower panel. The corresponding squares shown in the upper panel are the cross-correlation coefficients between vertical and radial components. These serve as indexes

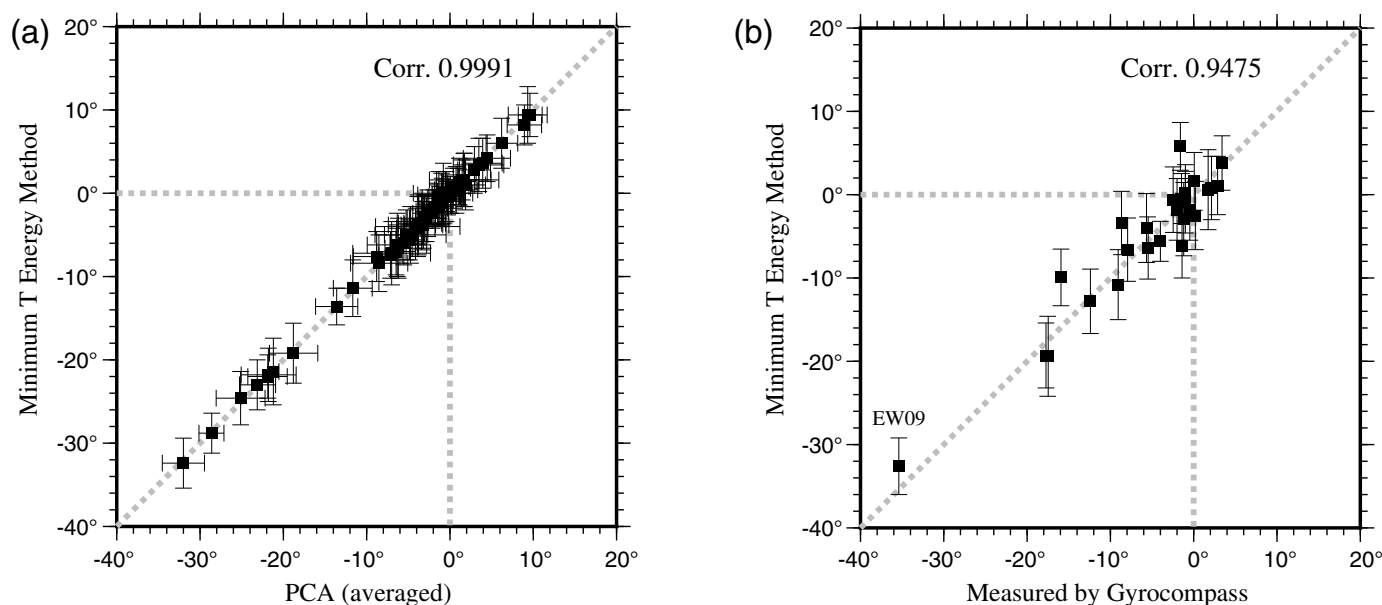




**▲ Figure 4.** An example showing the misorientation study using *P*-wave particle motion for station EW06. The upper left text indicates the station code, number of earthquakes used, result from minimizing transverse energy method with standard deviation, result from PCA method with standard deviation, and gyrocompass measurement. (a) Earthquakes used in this analysis. The different colors stand for the deviation between the single-earthquake PCA measurement and the average minimizing transverse energy measurement. (b) For a suite of events, the misorientation angle is determined by minimizing the summed energy of the transverse component. (c) The triangles represent the single-earthquake PCA measurement sorted by date, with earthquake magnitude and SNR shown in the lower panel. The corresponding squares in the upper panel are the cross-correlation coefficients between the vertical and radial components. This serves as indexes for the waveform quality and is expected to be close to one after the misorientation correction. For comparison, the minimizing transverse energy measurement is shown as a line. See text for details of the measurement. The color version of this figure is available only in the electronic edition.

for the waveform quality and are expected to be close to one. The average PCA measurement ( $\varphi_{PCA}$ ) is about  $3.8^\circ$  with standard deviation of  $3.1^\circ$ . Figure 4b shows the result of the minimizing transverse energy method. For a suite of events recorded by one station, we grid-search the misorientation angle from  $-90^\circ$  to  $90^\circ$  with an increment of  $0.1^\circ$ . We then determine the angle at which the summed *P*-wave energy on the transverse component reaches its minimum to be the misorientation angle of the station. The uncertainty is estimated using the method described in Niu and Li (2011), which defines

it as the 95% confidence level for one degree of freedom for each second of record. The minimizing transverse energy measurement ( $\varphi_{\min T}$ ) is  $3.7^\circ$  with  $3.4^\circ$  uncertainty and is shown as a line in comparison with the PCA method in Figure 4c. The gyrocompass measurement is  $3.43^\circ$ , which is very consistent with our estimations (Fig. 4). The distribution of earthquakes used in the study is shown in Figure 4a with varying shades representing the difference between the single-earthquake PCA and the minimizing transverse energy measurements. The regular pattern of the difference with respect to azimuth indi-



▲ **Figure 5.** Comparison of sensor misorientations obtained from our numerical analysis and those obtained from direct gyrocompass measurement. (a) Comparison between the PCA method and the minimizing transverse energy method for all stations. (b) Comparison between the minimizing transverse energy measurements with gyrocompass measurements (the station distributions correspond to the gray triangles and squares in Fig. 2). The numerical analysis and gyrocompass measurements are highly consistent with a correlation coefficient of 0.95.

icates that it is related to anisotropy or dipping structures beneath the station (see Discussion). The results for all of the stations in the NECsids Array are given in Table S1 (available in the electronic supplement to this article), with the average standard deviation being about  $3.6^\circ$ .

## DISCUSSION

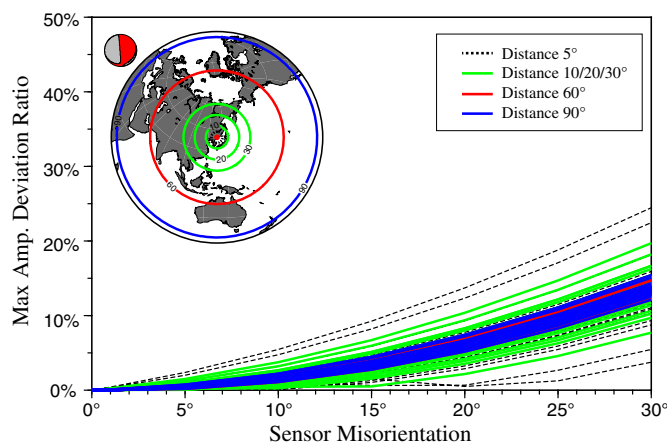
### Benchmark: Misorientation Measurement Using a Gyrocompass

To evaluate the reliability of the method, we directly measured the orientations for the NECsids Array stations (Fig. 2, gray triangles and squares) with a fiber-optic gyrocompass (North Finder NV-NF301 with an accuracy of  $\pm 0.3^\circ$ ) in May 2015 as a comparison with our numerical analysis. Most of the measurements were conducted at the location of the seismometer using an STS-2-rod to align the sensor with the gyrocompass. Because some sensors were located in narrow holes, the sensors' north direction was first marked on the ground and the orientation was subsequently measured, potentially increasing the error in the measurements. The gyrocompass measurements are also given in Table S1. As shown in Figure 5b, the misorientations determined in our study are very consistent with the gyrocompass measurements, with a correlation coefficient of 0.95. There is also high consistency between the  $\varphi_{\text{PCA}}$  and  $\varphi_{\text{min } T}$ , with a correlation coefficient larger than 0.99 (Fig. 5a). The high consistency between different methods indicates that the  $P$ -wave polarization method is robust and accurate to measure the sensor misorientation.

### Effect of Misorientation on Waveform

As previously mentioned, seismic sensor misorientation is a universal problem even for the global and national seismic networks operated by experienced field engineers. To study distortion of waveforms caused by misorientation, we generated synthetic seismograms to investigate the variation in  $P$ -wave amplitude on the radial component due to misorientation. We calculated synthetic seismograms using the 1D IASP91 model (Kennett and Engdahl, 1991) and spectral-element method (Nissen-Meyer *et al.*, 2014) (source and station distributions are shown in Fig. 6). We then rotated the R-T components off the great circle path up to  $30^\circ$  and filtered the waveform to 5–50 s. Next, we set a window for the radial-component waveform from  $-5$  to  $5$  s relative to the  $P$  wave and calculated the maximum amplitude deviation ratio (we define the ratio as  $|(Amp_{\text{max}} - Amp_{\text{max}}^{\text{misorientation}})| / |Amp_{\text{max}}|$ ) due to misorientation.

As shown in Figure 6, a  $10^\circ$  misorientation would cause an apparent 5% maximum amplitude change, and a  $30^\circ$  misorientation would cause an amplitude change as large as 25%. (Here we exclude the stations near the  $P$ -wave nodal direction, because the low  $P$ -wave amplitude would result in large uncertainty.) This suggests that it is impossible to correctly separate the  $P$ - $SV$  and  $SH$  energy without a sensor orientation correction when there is a large sensor misorientation. For true seismological studies, one needs to consider additional concerns such as the combined effect on station distribution or azimuth coverage from misorientation at each station. The uncertainty range from our  $P$ -wave polarization analysis is  $3^\circ$ – $4^\circ$ , consistent



▲ **Figure 6.** The maximum amplitude changes for the direct  $P$ -wave on the radial component due to sensor misorientation. We generate synthetic seismograms with the 1D IASP91 model with stations distributed over a full azimuth and  $5^{\circ}$ – $90^{\circ}$  epicentral distances. The various colors indicate different epicentral distances. See text for details on the effects of misorientation on amplitude. The color version of this figure is available only in the electronic edition.

with that of Ekström and Busby (2008). Given the effects of the anisotropy, dipping interface (see [Effect of Anisotropy and Dipping Interface](#)), and the  $P$ -wave amplitude deviation ratio, we would stress that effort should be made to orient sensors within an error of  $3^{\circ}$ .

### The Minimum Required Earthquake Number

The measurements in this study are based on a large dataset; however, most temporary seismic experiments have an operation duration of around one year. Is it possible to offer reliable misorientation measurements with the data available from just one year? In this section, we analyzed the minimum number of earthquakes that are required for a stable measurement using the bootstrapping method (Efron and Tibshirani, 1991). In each bootstrapping session, we randomly select  $m$  earthquakes from the original database consisting of  $M$  earthquakes ( $m \leq M$ ), allowing duplicates. We then estimate the sensor misorientation for each new dataset. The mean misorientation is obtained as the average of the trials,  $\varphi = 1/N \sum_{i=1}^N \varphi_i$ , in which  $N$  is the number of the bootstrapping trials ( $N = 200$  for this study). As shown in Figure 7, the uncertainty decreases as more earthquakes are used in the estimation. When the earthquake number is greater than 10, the results become stable and reach to the level of using all events. According to the USGS statistics, the average number of the earthquakes worldwide with magnitude greater than 6.0 is greater than 150 per year. After filtering for epicenter distance and excluding earthquakes with low SNR and linear particle motion, we would still expect to record more than 10 events within epicentral distance range of  $5^{\circ}$ – $90^{\circ}$  per year at any station, which would be enough for a robust estimation using the  $P$ -wave polarization method.

### Effect of Anisotropy and Dipping Interface

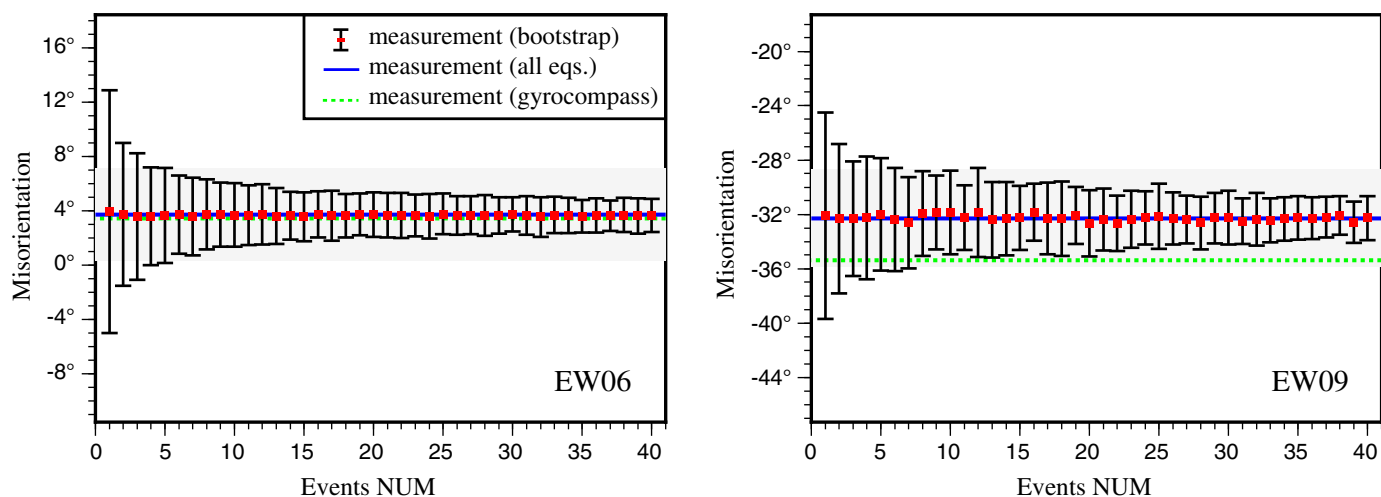
As mentioned earlier, the  $P$ -wave polarization analysis assumes an ideal Earth with a homogeneous and isotropic layered structure. In such an ideal case, the angle of sensor misorientation should be constant and independent of the azimuth of the incoming waves. However, in the real Earth, the inferred sensor misorientation can be biased by several other factors, such as seismic anisotropy and a dipping interface beneath the station. These factors can introduce deviations in  $P$ -wave polarization, which can strongly depend on the azimuth of the incoming waves. Because earthquakes are located at various azimuths and distances, the pattern of azimuthal dependence (e.g., Fig. 4a) indicates that the 3D structure beneath the station is likely related to such features.

Here, we evaluated the effects of anisotropy and dipping interfaces by generating synthetic seismograms for anisotropic and dipping models. We used a ray-based algorithm developed by Frederiksen and Bostock (2000) to generate teleseismic synthetic waveforms in a dipping anisotropic medium. We used the strike and dip angle to describe the dipping interface (Fig. 8a). For anisotropy, we studied the case of hexagonally symmetric anisotropy, which can be fully described with five elastic parameters (Levin and Park, 1997, 1998). These parameters are related to the strength of  $P$ - and  $S$ -wave anisotropy, the trend and plunge of the anisotropic symmetry, and  $\eta$ , which defines the shape of the velocity ellipsoid (Levin and Park, 1998; Frederiksen and Bostock, 2000) (Fig. 9a). In this study, we assumed the velocity ellipsoid to be purely ellipsoidal, such that  $\eta$  becomes a function of the percent of anisotropy, as assumed in several previous studies (Levin and Park, 1998; Sherrington et al., 2004; Porter et al., 2011).

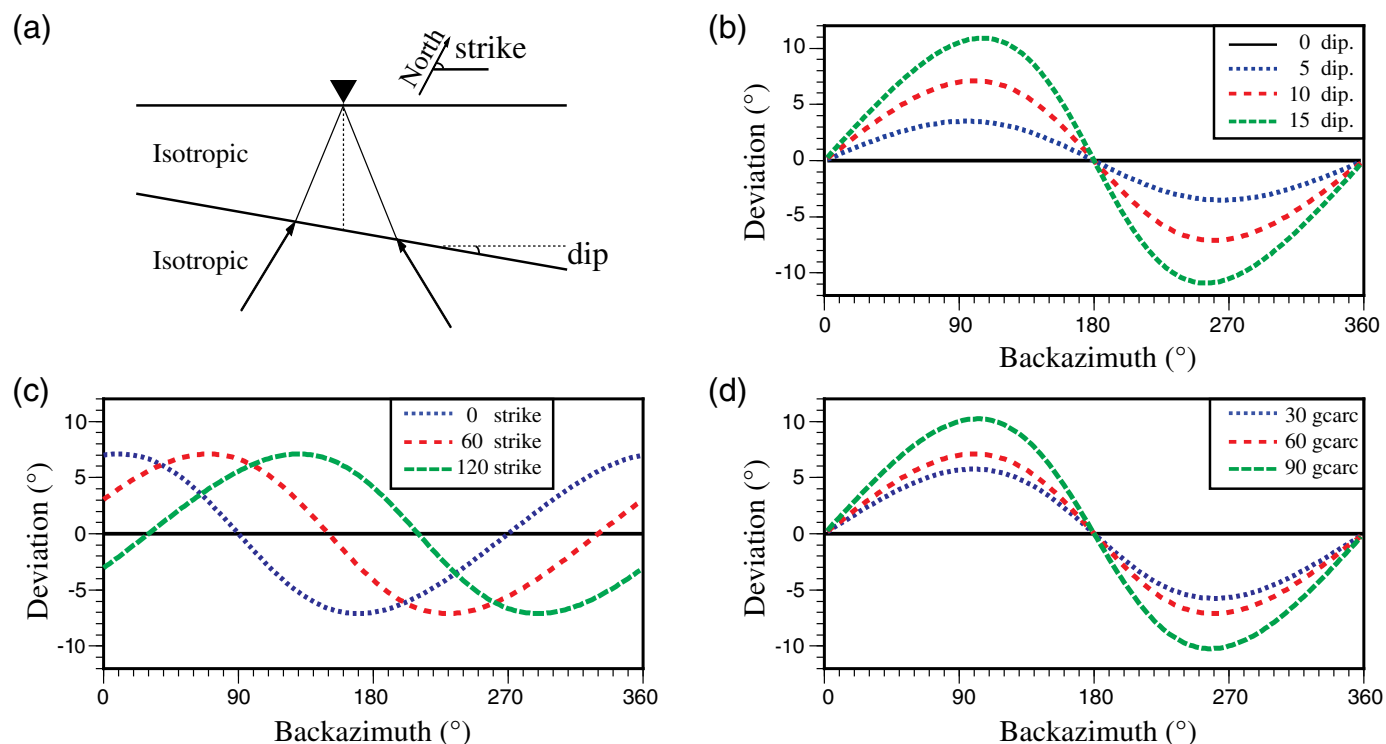
As shown in Table 1, we mainly tested two types of models, one with a dipping interface and one with slow-unique axis anisotropy in the crust. We generated synthetic seismograms for different models with rays coming from different back azimuths. We computed the  $P$ -wave polarization for the synthetic seismograms in the same manner as the data and plotted the results as a function of back azimuth (Figs. 8 and 9).

The results from testing the dipping interface indicate a two-lobed curve with a  $360^{\circ}$  periodicity (Fig. 8b). The change of the strike of the interface produces a phase shift (Fig. 8c), whereas the dip angle and epicentral distance will influence the amplitude of deviation (Fig. 8b,d). The effect of the dipping interface comes from the conversion of  $P$ – $SH$  waves across the interface. For a  $15^{\circ}$  dipping Moho, the maximum deviation is around  $10^{\circ}$ . Fortunately, the Moho interface is relatively flat in most locations. For a  $15^{\circ}$  dipping Moho, the depth change over a 100 km horizontal distance would be as much as 26 km, which is not the case for most regions. Therefore, the influence of a dipping structure is expected to be relatively small for our  $P$ -wave polarization analysis.

In the simplest layered anisotropic medium with a horizontal symmetry axis, the result shows a four-lobed curve with a  $180^{\circ}$  periodicity (Fig. 9b). Different trend (fast-axis) directions produce similar patterns but with a phase shift (Fig. 9c). Rays coming from different epicentral distances show negli-



▲ **Figure 7.** Bootstrapping for the minimum number (NUM) of earthquakes required for robust misorientation estimation. We can obtain a stable measurement using at least 10 earthquakes in our analysis. The locations of these two stations are shown in Figure 2. The EW09 is the station with the largest misorientation, as shown in Figure 5b. The color version of this figure is available only in the electronic edition.

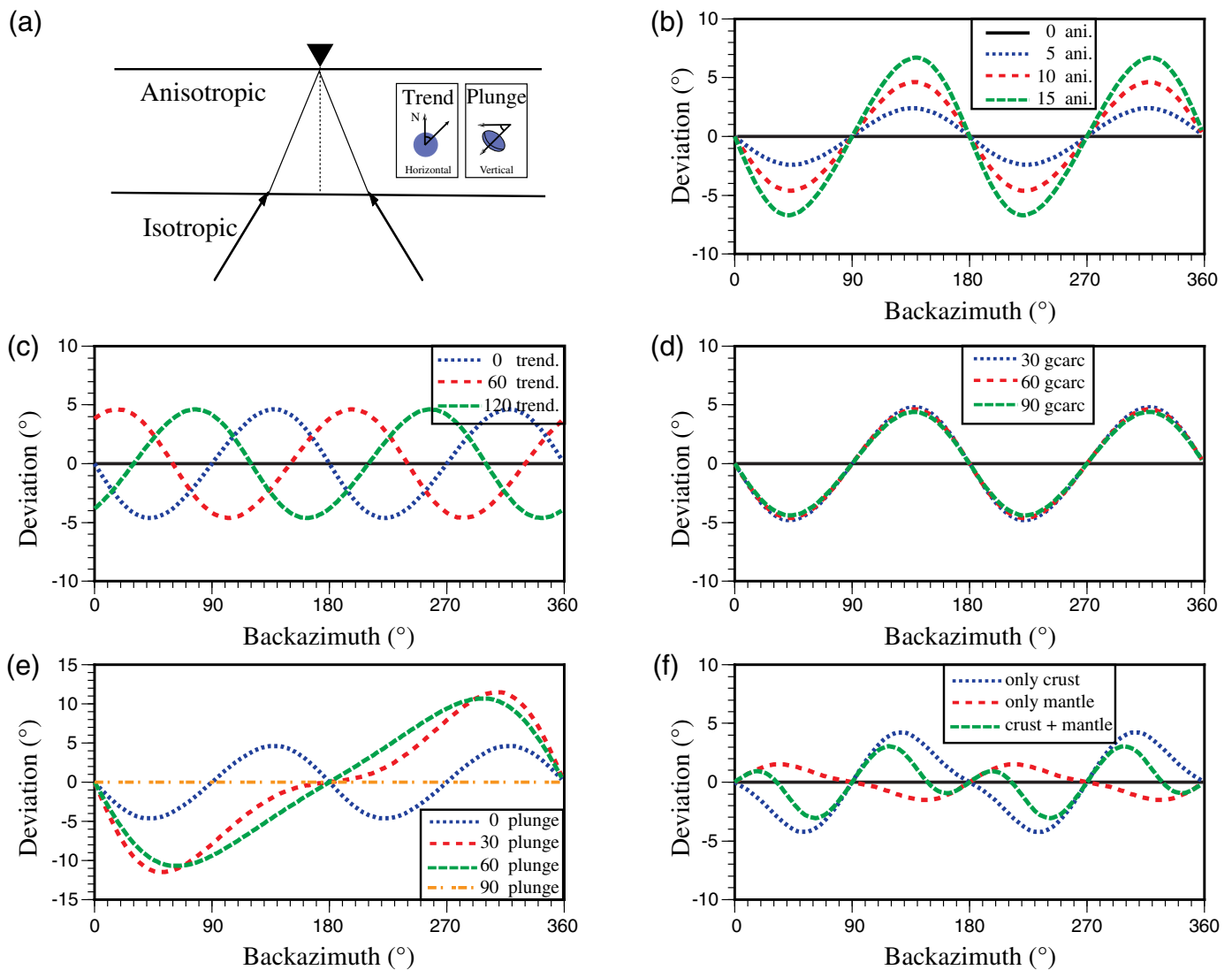


▲ **Figure 8.** The effect of a dipping structure on particle motion in an isotropic medium, shown as a function of back azimuth of the incoming ray. (a) The dipping structure, (b) sensitivity to the dip angle, (c) sensitivity to the strike angle, and (d) sensitivity to the epicentral distance (incident angle). The corresponding models are described in Table 1, in which (b), (c), and (d) correspond to models M1, M2, and M3, respectively. The color version of this figure is available only in the electronic edition.

gible variations (Fig. 9d). A change in plunge of the anisotropic symmetry axis causes a deviation pattern in between the cases of the isotropic dipping interface and horizontal symmetry axis but with a larger amplitude than that of the horizontal axis anisotropy (Fig. 9e). With a plunge around 90°, the pattern

converges to that of the isotropic case. We primarily tested slow-unique axis anisotropy, which is often assumed for crustal anisotropy studies. However, the effects of fast-unique axis anisotropy are similar. We also tested a model with two anisotropic layers corresponding to the crust and the upper mantle





▲ **Figure 9.** The effect of anisotropy on particle motion in a hexagonally symmetric medium shown as a function of back azimuth of the incoming ray. (a) The anisotropic medium, (b) sensitivity to the strength of anisotropy, (c) sensitivity to the trend, (d) sensitivity to the epicentral distance (incident angle), (e) sensitivity to the plunge given a fixed strength and trend, and (f) multilayer anisotropy effect. The corresponding models are described in Table 1, in which (b), (c), (d), (e), and (f) correspond to models M4, M5, M6, M7, and M8, respectively. The color version of this figure is available only in the electronic edition.

(Table 1, model M8). For two layers with the same strength of horizontal anisotropy but different fast axis, the deviation is dominated by the top layer (Fig. 9f). A thorough discussion of multiple layer anisotropy influence is beyond the scope of this article. However, the influence of anisotropy is a local effect within the range of one wavelength, and more complex patterns of deviations are possible with multiple layer anisotropy (Schulte-Pelkum *et al.*, 2001; Schulte-Pelkum and Blackman, 2003).

Seismic anisotropy is a fundamental characteristic feature of the Earth (Mainprice, 2007). *P*-wave propagation in anisotropic media produces a quasi-*P* wave where particle motion is not parallel to the propagation direction (Crampin *et al.*, 1982). Algebraic analyses and numerical experiments show that

the deviation is less than 7° for even very strongly (30%) anisotropic material (Crampin, 1981; Crampin *et al.*, 1982). From petrophysical modeling of *P*-wave polarization in minerals and rocks, the deviation is shown to be less than 5° for 10% anisotropic media (Schulte-Pelkum and Blackman, 2003). For the range of anisotropic values postulated from observations for the crust and uppermost mantle (less than 10%; Savage, 1999), the influence of anisotropy on misorientation estimates is found to be relatively small.

In general, if the earthquakes provide a good azimuthal coverage, we can identify the pattern and average out the impact of anisotropy and dipping interfaces. In another sense, with good azimuthal coverage, we can also use *P*-wave polarization measurements to analyze the anisotropy or dipping

**Table 1**  
**Model Parameters for Synthetic Tests of Anisotropy and Dipping Interfaces**

Model	<i>H</i>	$\rho$	$V_P$	$V_S$	Anisotropy			Dipping Layer	
	(km)	(g/cm <sup>3</sup> )	(km/s)	(km/s)	Anisotropy (%)	Trend (°)	Plunge (°)	Strike (°)	Dip (°)
M1	33.0	2.92	6.50	3.75	—	—	—	90	0/5/10/15
	—	3.32	8.04	4.47	—	—	—	—	—
M2	33.0	2.92	6.50	3.75	—	—	—	0/60/120	10
	—	3.32	8.04	4.47	—	—	—	—	—
M3	33.0	2.92	6.50	3.75	—	—	—	90	10
	—	3.32	8.04	4.47	—	—	—	—	—
M4	33.0	2.92	6.50	3.75	0/−5/−10/−15	0	0	—	—
	—	3.32	8.04	4.47	—	—	—	—	—
M5	33.0	2.92	6.50	3.75	−10	0/60/120	0	—	—
	—	3.32	8.04	4.47	—	—	—	—	—
M6	33.0	2.92	6.50	3.75	−10	0	0	—	—
	—	3.32	8.04	4.47	—	—	—	—	—
M7	33.0	2.92	6.50	3.75	−10	0	0/30/60/90	—	—
	—	3.32	8.04	4.47	—	—	—	—	—
M8	33.0	2.92	6.50	3.75	−10	0	0	—	—
	92.8	3.50	8.03	4.36	10	0	0	—	—
	134.0	3.50	8.03	4.36	—	—	—	—	—
	—	3.65	8.20	4.48	—	—	—	—	—

Layers are listed from top to bottom. The bottom layer is assumed to be a half-space. Slashes indicate different cases in Figures 8 and 9, and dashes (—) indicate the data not available.

structure under a seismic station. For example, Schulte-Pelkum *et al.* (2001) and Fontaine *et al.* (2009) used long-period *P*-wave polarization to measure upper-mantle anisotropy, which can be combined with other seismic studies such as *SKS* measurements to give a better constraint on anisotropy and dipping structure.

## CONCLUSIONS

Concerns of sensor misorientation in global and national seismic stations have been noted in many previous studies (Ekström and Busby, 2008; Niu and Li, 2011; Ringler *et al.*, 2013; Rueda and Mezcuca, 2015). In this study, we examined the epoch-dependent sensor misorientation for our temporary seismic array (NECsaid's Array) using *P*-wave particle motion. The misorientation values estimated by analyzing *P*-wave particle motion (PCA and the minimizing transverse energy method) are highly consistent with the gyrocompass measurements. We discuss various parameters (SNR, particle motion linearity, the minimum number of earthquakes) that improve the accuracy of the fast-automatic analysis. Finally, we discuss factors, such as seismic anisotropy and dipping structure, that can influence our analysis. Our results show the effects from anisotropy or a dipping interface vary periodically with back azimuth and, therefore, have limited influence on our misorientation measurement. With good azimuthal coverage, the *P*-wave particle motion method could also be used to study anisotropy or dipping structure beneath the seismic stations.

Finally, this study will help to provide a well-documented epoch-dependent analysis of misorientation for existing databases, and aimed to increase awareness of misorientation when installing permanent or temporary stations.

## DATA AND RESOURCES

The NECsaid's Array was deployed by the key project 41130416 and the general project 41474041 funded by the National Natural Science Foundation of China (NSFC). The NECsaid's Array data from 2011 to 2014 will be available to share after three years from the end of the NSFC 41130416 project (<http://www.seislab.cn/>, last accessed April 2016). Data used in this study are available from us upon request. The earthquake catalog was retrieved from the International Seismological Centre website (<http://www.isc.ac.uk>, last accessed January 2016). Sac2000 (Goldstein *et al.*, 2003), Taup (Crotwell *et al.*, 1999), and Generic Mapping Tools (GMT) (Wessel *et al.*, 2013) were used for basic data processing and figure development. ☒

## ACKNOWLEDGMENTS

The research is supported by the National Science Foundation of China (41130316, 41474041, and 41274065). We thank all the people in the NECsaid's Array project for installing and servicing the seismic array. We also thank Hebei Earthquake Administration for providing the gyrocompass (North Finder

NV-NF301) in May 2015 to make it possible to measure the sensor misorientation directly. We would like to especially thank Fenglin Niu for providing the *P*-wave particle motion analysis code. We greatly appreciate the editors and three anonymous reviewers for their constructive comments. We are also very grateful to Valère Lambert and Anna Foster, who, as native speakers, helped us improve the article.

## REFERENCES

- Bormann, P. (2012). *New Manual of Seismological Observatory Practice (NMSOP-2)*, IASPEI, GFZ German Research Centre for Geosciences, Potsdam, Germany.
- Crampin, S. (1981). A review of wave motion in anisotropic and cracked elastic-media, *Wave Motion* **3**, 343–391.
- Crampin, S., R. A. Stephen, and R. McGonigle (1982). The polarization of *P*-waves in anisotropic media, *Geophys. J. Roy. Astron. Soc.* **68**, 477–485.
- Crotwell, H. P., T. J. Owens, and J. Ritsema (1999). The TauP Toolkit: Flexible seismic travel-time and ray-path utilities, *Seismol. Res. Lett.* **70**, 154–160.
- Efron, B., and R. Tibshirani (1991). Statistical-data analysis in the computer-age, *Science* **253**, 390–395.
- Ekström, G., and R. W. Busby (2008). Measurements of seismometer orientation at USArray transportable array and backbone stations, *Seismol. Res. Lett.* **79**, 554–561.
- Fontaine, F. R., G. Barruol, B. L. N. Kennett, G. H. R. Bokelmann, and D. Reymond (2009). Upper mantle anisotropy beneath Australia and Tahiti from *P* wave polarization: Implications for real-time earthquake location, *J. Geophys. Res.* **114**, no. B03306, doi: [10.1029/2008JB005709](https://doi.org/10.1029/2008JB005709).
- Frederiksen, A. W., and M. G. Bostock (2000). Modelling teleseismic waves in dipping anisotropic structures, *Geophys. J. Int.* **141**, 401–412.
- Goldstein, P., D. Dodge, M. Firpo, and L. Minner (2003). SAC2000: Signal processing and analysis tools for seismologists and engineers, in *The LASPEI International Handbook of Earthquake and Engineering Seismology*, W. H. K. Lee, H. Kanamori, P. C. Jennings, and C. Kisslinger (Editors), Chapter 85.5, Academic Press, San Diego, California, Vol. 81, 1613–1620.
- Jurkevics, A. (1988). Polarization analysis of three-component array data, *Bull. Seismol. Soc. Am.* **78**, 1725–1743.
- Kennett, B. L. N., and E. R. Engdahl (1991). Traveltimes for global earthquake location and phase identification, *Geophys. J. Int.* **105**, 429–465.
- Laske, G. (1995). Global observation of off-great-circle propagation of long-period surface-waves, *Geophys. J. Int.* **123**, 245–259.
- Lay, T., and T. C. Wallace (1995). *Modern Global Seismology*, Academic Press, San Diego, California.
- Levin, V., and J. Park (1997). *P*–*SH* conversions in a flat-layered medium with anisotropy of arbitrary orientation, *Geophys. J. Int.* **131**, 253–266.
- Levin, V., and J. Park (1998). *P*–*SH* conversions in layered media with hexagonally symmetric anisotropy: A cookbook, *Pure Appl. Geophys.* **151**, 669–697.
- Lockman, A. B., and R. M. Allen (2005). Single-station earthquake characterization for early warning, *Bull. Seismol. Soc. Am.* **95**, 2029–2039.
- Mainprice, D. (2007). Seismic anisotropy of the deep Earth from a mineral and rock physics perspective, in *Treatise in Geophysics*, S. G. Price (Editor), First Ed., Vol. 2, Mineral Physics, Elsevier, Oxford, United Kingdom, 437–492.
- Nissen-Meyer, T., M. van Driel, S. C. Stahler, K. Hosseini, S. Hempel, L. Auer, A. Colombi, and A. Fournier (2014). AxiSEM: Broadband 3-D seismic wavefields in axisymmetric media, *Solid Earth* **5**, 425–445.
- Niu, F., and J. Li (2011). Component azimuths of the CEArray stations estimated from *P*-wave particle motion, *Earthq. Sci.* **24**, 3–13.
- Niu, F., T. Bravo, G. Pavlis, F. Vernon, H. Rendon, M. Bezada, and A. Levander (2007). Receiver function study of the crustal structure of the southeastern Caribbean plate boundary and Venezuela, *J. Geophys. Res.* **112**, 15.
- Noda, S., S. Yamamoto, S. Sato, N. Iwata, M. Korenaga, and K. Ashiya (2012). Improvement of back-azimuth estimation in real-time by using a single station record, *Earth Planets Space* **64**, 305–308.
- Porter, R., G. Zandt, and N. McQuarrie (2011). Pervasive lower-crustal seismic anisotropy in southern California: Evidence for underplated schists and active tectonics, *Lithosphere* **3**, 201–220.
- Ringler, A. T., C. R. Hutt, K. Persefield, and L. S. Gee (2013). Seismic station installation orientation errors at ANSS and IRIS/USGS stations, *Seismol. Res. Lett.* **84**, 926–931.
- Rost, S., and C. Thomas (2002). Array seismology: Methods and applications, *Rev. Geophys.* **40**, 27.
- Rueda, J., and J. Mezcuca (2015). Orientation analysis of the Spanish Broadband National Network using Rayleigh-wave polarization, *Seismol. Res. Lett.* **86**, 929–940.
- Savage, M. K. (1999). Seismic anisotropy and mantle deformation: What have we learned from shear wave splitting? *Rev. Geophys.* **37**, 65–106.
- Schulte-Pelkum, V., and D. K. Blackman (2003). A synthesis of seismic *P* and *S* anisotropy, *Geophys. J. Int.* **154**, 166–178.
- Schulte-Pelkum, V., G. Masters, and P. M. Shearer (2001). Upper mantle anisotropy from long-period *P* polarization, *J. Geophys. Res.* **106**, 21,917–21,934.
- Sherrington, H. F., G. Zandt, and A. Frederiksen (2004). Crustal fabric in the Tibetan plateau based on waveform inversions for seismic anisotropy parameters, *J. Geophys. Res.* **109**, 22.
- Wessel, P., W. H. Smith, R. Scharroo, J. Luis, and F. Wobbe (2013). Generic Mapping Tools: Improved version released, *Eos Trans. AGU* **94**, 409–410.
- Zha, Y., S. C. Webb, and W. Menke (2013). Determining the orientations of ocean bottom seismometers using ambient noise correlation, *Geophys. Res. Lett.* **40**, 3585–3590.

Xin Wang  
Qi-Fu Chen  
Juan Li

Key Laboratory of Earth and Planetary Physics  
Institute of Geology and Geophysics  
Chinese Academy of Sciences (IGGCAS)  
No. 19, Beitucheng Western Road  
Chaoyang District  
Beijing 100029  
P. R. China  
[chenqf@mail.iggcas.ac.cn](mailto:chenqf@mail.iggcas.ac.cn)  
[wangxin@mail.iggcas.ac.cn](mailto:wangxin@mail.iggcas.ac.cn)  
[juanti@mail.iggcas.ac.cn](mailto:juanti@mail.iggcas.ac.cn)

Shengji Wei<sup>1</sup>  
Earth Observatory of Singapore (EOS)  
Nanyang Technological University  
50 Nanyang Avenue  
Block N2-01a-15  
Singapore 639798, Singapore  
[shijiwei@ntu.edu.sg](mailto:shijiwei@ntu.edu.sg)

Published Online 18 May 2016

<sup>1</sup> Also at Asian School of Environment (ASE), Nanyang Technological University, 50 Nanyang Avenue, Block N2-01a-15, Singapore 639798, Singapore.